An architecturally rational hemostat for rapid stopping of massive bleeding on anticoagulation therapy

Vivian K. Lee[a,b,c,d], Taewoo Lee[a,b,c,d,1], Amrit Ghosh[a,d,1] (ID), Tanmoy Saha[a,d,1], Manish V. Bais[b,e], Kala Kumar Bharani[f], Milan Chag[g], Keyur Parikh[g], Parloop Bhatt[g], Bumseok Namgung[a,b,c,d], Geethapriya Venkataramanan[a,d], Animesh Agrawal[h], Kiran Sonaje[h], Leo Mavely[h,i], Shiladitya Sengupta[a,d], Raghunath Anant Mashelkar[j,2], and Hae Lin Jang[a,b,c,2]

Hemostatic devices are critical for managing emergent severe bleeding. With the increased use of anticoagulant therapy, there is a need for next-generation hemostats. We rationalized that a hemostat with an architecture designed to increase contact with blood, and engineered from a material that activates a distinct and undrugged coagulation pathway can address the emerging need. Inspired by lung alveolar architecture, here, we describe the engineering of a next-generation single-phase chitosan hemostat with a tortuous spherical microporous design that enables rapid blood absorption and concentrated platelets and fibrin microthrombi in localized regions, a phenomenon less observed with other classical hemostats without structural optimization. The interaction between blood components and the porous hemostat was further amplified based on the charged surface of chitosan. Contrary to the dogma that chitosan does not directly affect physiological clotting mechanism, the hemostat induced coagulation via a direct activation of platelet Toll-like receptor 2. Our engineered porous hemostat effectively stopped the bleeding from murine liver wounds, swine liver and carotid artery injuries, and the human radial artery puncture site within a few minutes with significantly reduced blood loss, even under the anticoagulant treatment. The integration of engineering design principles with an understanding of the molecular mechanisms can lead to hemostats with improved functions to address emerging medical needs.

clotting | hemostasis | trauma | biomaterial | hemostat

Uncontrolled bleeding accounts for approximately 35% of more than 5 million trauma deaths globally each year (1, 2). The risk of hemorrhage and the difficulty of hemostasis is further aggravated when individuals are on anticoagulant therapies (3, 4). In the United States alone, more than 11 million people are taking anticoagulation medications to treat myocardial infarction, strokes, and thromboembolic complications (5). This leads to a concerning increase in emergency visits due to bleeding complications, including skin and wound bleeding, marking a growing health issue (6). However, it is extremely challenging to screen prescription information of the bleeding patients and provide appropriate anticoagulation reversal agents during sudden emergency situations.

External hemostatic dressings were developed to rapidly control massive bleeding as first-line emergency care. An ideal hemostat would induce immediate and effective hemostasis even in the most extreme bleeding conditions. Hemostasis should be maintained for several hours after the initial application of the hemostat until clinical treatment is available, and at that time, the hemostat should be easily removable without damaging the tissue or leaving any toxic residues. Long-stable shelf life, ease of storage, high portability, ease of use with minimal preparation, and good biocompatibility are also required (7, 8). In addition, the ability of hemostats to specifically target patients under anticoagulant therapy would notably contribute to the field, addressing a clear need in a growing patient population. To date, no single hemostatic agent or dressing completely meets all these criteria (7, 9).

To address the above emergent needs, we reasoned that a next-generation hemostat should meet two necessary criteria: First, its architectural design should increase contact with blood clotting components. Second, it should be engineered from a material that activates a distinct and undrugged coagulation pathway, enabling clotting independent of the anticoagulant therapy a patient may be undergoing. However, the majority of hemostats currently used in the clinics are simple constructs with kaolin ($Al_2O_3 \cdot 2SiO_2 \cdot 2H_2O$) clay mineral or chitosan in powder form or impregnated in gauzes. While kaolin quickly absorbs water and initiate physiological coagulation cascade by activating factor XII (9–11), it is postulated that the exceptionally highly positive charge of chitosan captures negatively charged blood components such as platelets, fibrinogen, red blood cells, etc. (12), and

Significance

Approximately 35% of hemorrhagic deaths occur before hospital arrival, with the risk amplified by anticoagulant therapies. To address this, our research introduces a next-generation chitosan hemostat, rationally designed with optimized pore size and connectivity. This design allows the hemostat to quickly absorb blood and concentrate clotting components, effectively counteracting anticoagulant effects. Contrary to previous beliefs that chitosan does not participate in the physiological clotting process, we identified its direct role in activating platelets via the TLR-2 (Toll-like receptor 2), thereby initiating the coagulation cascade in the presence of currently approved anticoagulants. This study presents an approach in hemostat development for emergency care, especially valuable for patients on anticoagulants.

thereby facilitates clotting independent of the physiological clotting mechanism (9, 13). However, such powder-impregnated hemostats face several limitations: First, there is no architectural optimization to facilitate enhanced interaction with blood components. Second, powder easily detaches from the gauze and can be washed away during heavy bleeding (14). Third, residual powders can cause undesirable coagulation and complications away from the wound site (9, 14).

Here, we describe the rational engineering of an architecturally optimized hemostat, inspired by the tortuous porous lung alveoli that achieves a high interaction rate with blood within a short time (Fig. 1 *A* and *B*). Indeed, computational simulations showed that the modifications in porous structures can result in increasing/decreasing fluid dynamics factors with an inverted relationship of factors related to the accumulation of particles (i.e., platelets). In parallel, we demonstrate that chitosan can activate platelets via Toll-like receptor 2 (TLR2), a pathway distinct from those targeted by the currently approved anticoagulant drugs, such as aspirin, eptifibatide, clopidogrel, cangrelor, and vorapaxar, which block the activation of platelets by inhibiting thromboxane, integrin $\alpha_{IIb}\beta_3$ receptor, purinergic receptor (P2Y$_{12}$), and protease-activated receptor (PAR). This finding of a direct pharmacological effect of chitosan contrasts with the accepted dogma that it does not directly interact with the physiological clotting mechanism (9, 13, 15) but more importantly posits its functionality as an effective hemostatic material in the presence of anticoagulant therapeutics.

Based on these findings, we engineered single-phase chitosan scaffolds with various porous structures, including different sphericities of pores, and experimentally validated the modeling predictions. In comparative studies involving hemostats with tortuous and spherical porous structures, fibrous structures, and small oblate porous structures, we observed consistency between in silico predictions and ex vivo and in vivo observations. More spherical pores demonstrated faster liquid absorption compared to oblate porous structures. The rapid blood absorption flow in the spherical pores entrapped more platelets within the material than in fibrous structures. Consequently, the spherical porous structure enhanced the overall hemostatic performance compared to both fibrous and small oblate porous structures. We demonstrated the efficacy of the engineered chitosan hemostat in various models of severe vascular injuries, including injury sites of murine and swine livers, an organ that is highly vascularized and presents with excessive bleeding on injury, swine carotid artery dissection, and in a clinical study in a human patient radial artery bleeding setting, where anticoagulants are administered to prevent clotting. The integration of an optimal architectural design with a material that activates an undrugged target in the coagulation machinery opens a paradigm in engineering hemostats that can address the emerging need of managing massive hemorrhage in patients on currently approved anticoagulant therapies.

Results

Simulating Fluid Absorption and Platelet Accumulation Features.
Rapid absorption is a vital quality for hemostatic agents as it allows swift concentration of clotting components at the bleeding sites (16) and creates high shear zones that accelerate platelet activation and aggregation (17, 18). Such capacity for rapid and voluminous blood absorption has been achieved primarily by introducing new materials or modifying the chemical properties of existing materials (7, 16). Another promising approach is altering material microstructures, which can also impact the liquid absorption speed and capacity (19). Indeed, studies demonstrated that hemostats equipped with built-in microchannels can increase blood

absorption rate (20, 21). Here, we further posited that tortuous porous structure with optimized size and shape of pores could improve the filtration capacity of the hemostat, capturing and concentrating platelets more effectively to achieve rapid primary hemostasis (Fig. 1*C*). These tortuous porous structures, similar to lung alveoli, employ a depth filtration mechanism (22). To test the hypothesis, we created theoretical models of various porous structures with varying diameters, sphericity, and overlap ratios of pores (Fig. 1 *D–I* and *SI Appendix*, Fig. S1).

We categorized factors that are involved in hemostatic mechanisms into two groups: based on fluid absorption and particle accumulation. Fluid factors such as fluid shear rate and flow diffusivity affect the absorption speed of materials. Particle factors are related to the accumulation of blood clotting components, such as platelets, the essential initiators of the clotting cascade. Increasing pore diameter led to the higher fluid shear rate (Fig. 1 *D* and *G*) with a more aligned flow direction (Fig. 1*I*). The same tendency was observed with increasing pore sphericity (Fig. 1 *F*, *G*, and *I*) and increasing pore overlap ratio (*SI Appendix*, Fig. S1*C*). Conversely, particle residence time showed an inverse correlation with these fluid factors. As the fluid shear rate increased, particles passed more quickly through the porous structures (Fig. 1 *E* and *H*), covering less traveling distance within the materials (*SI Appendix*, Fig. S1*D*). Interestingly, when pore size was too small, particles struggled to rapidly enter the porous structure. This can lead to real-world scenarios where blood leaks from the surface of the hemostatic material, carrying clotting components away, rather than promoting their absorption and accumulation within the hemostatic material.

Engineering an Alveolar Chitosan Structure.
To test the simulation results, we next engineered hemostats with controlled porous "alveolar" structures. We chose chitosan as the base material due to its excellent basic hemostatic performance and morphological flexibility (23, 24), and as described later, its ability to activate the coagulation machinery via a mechanism independent of the currently drugged pathways. Chitosan is derived from the deacetylation process of chitin [β-(1-4)-N-acetyl-D-glucosamine], which is the second most abundant polysaccharide in nature and can be found in crustacean shells (25). The surface of chitosan becomes positively charged during the deacetylation process, which can be further protonated by treating with acidic chemicals such as acetic acid that hydrogenate amino groups ($-NH_2 \rightarrow -NH_3^+$).

We rationalized that a single-phase chitosan structure instead of the current practice of embedding chitosan microparticles on fibers can overcome the problem of chitosan powder dislodging from the structure. A porous structured chitosan pad was prepared by lyophilizing chitosan (2% w/v) dissolved in dilute acetic acid, which induced phase separation of the solvent crystals from chitosan suspension during the temperature decrease and then generated porous structured chitosan after the removal of frozen solvent crystals. Highly deacetylated chitosan with a high molecular weight and a narrow polydispersity was used to precisely regulate the polymer solubility at a given temperature and achieve a highly integrated structure based on the entanglement of long polymeric chains (*SI Appendix*, Fig. S2 *A* and *B*). On the other hand, chitosan with a broad polydispersity generates uncontrolled partial crystallization of polymer from different levels of molecular weight, resulting in the formation of various sizes of pores and disintegrated polymeric pieces. The uniform porosity and homogeneous cavity size distribution of engineered porous chitosan pads were confirmed by microCT (Fig. 1*B*) and FESEM (Field emission scanning electron microscope) (Fig. 2*A*). The single-phase porous chitosan hemostatic pads had a more stable structure and
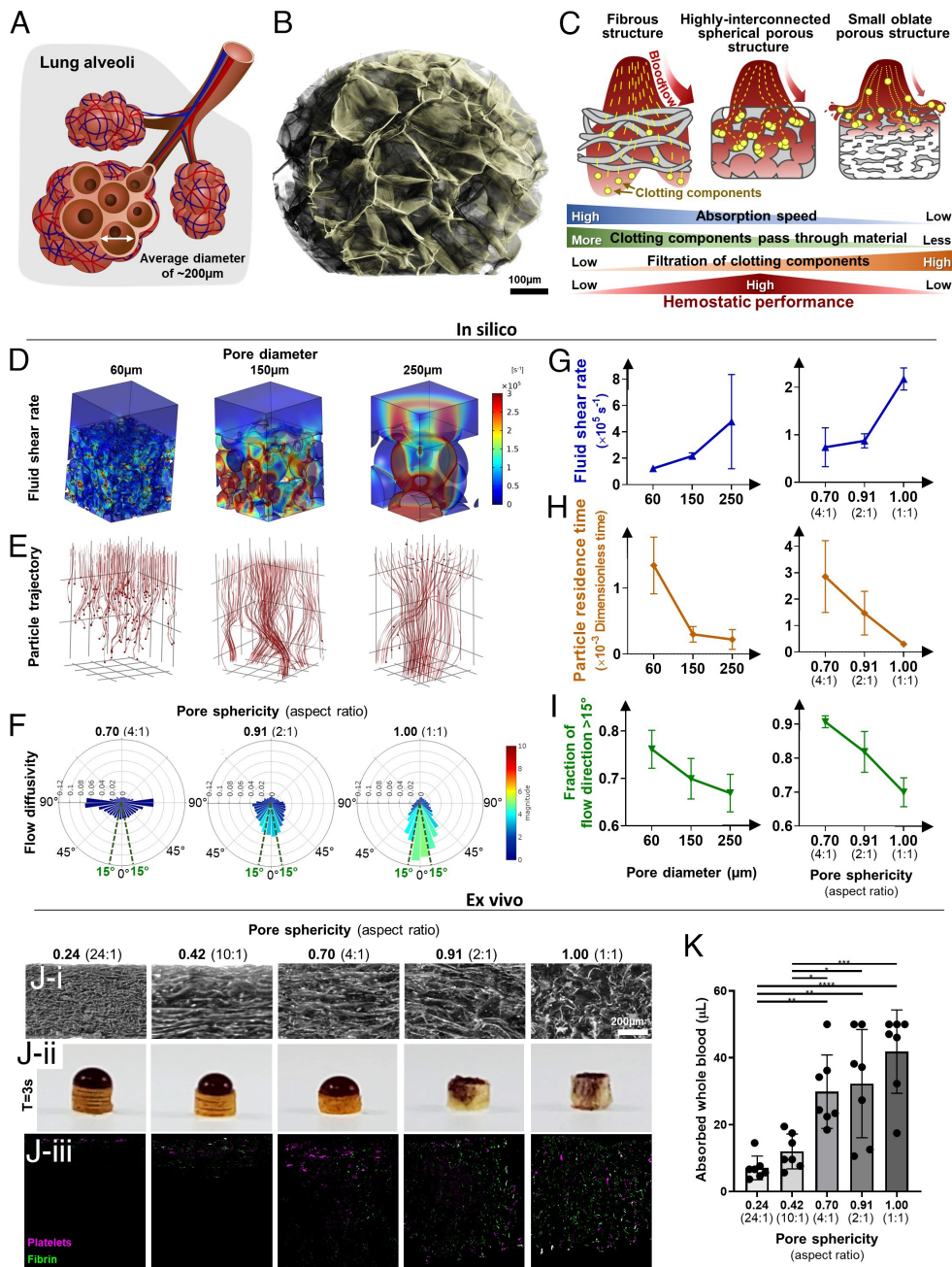
Fig. 1. Porous structures of hemostatic materials affect blood absorption and clotting component accumulation. (*A*) A schematic of lung alveoli with an assembled structure consisting of millions of microballoon-like air sacs that facilitate rapid interaction with blood. (*B*) 3D reconstructed microCT image of the engineered porous chitosan pad. (*C*) Schematic diagram of maximizing the hemostatic performance of the porous material by balancing its blood absorption speed and accumulation of blood clotting components. (*D*) Fluid shear rate distribution in computational porous structures with varying pore diameters. (*E*) Particle trajectory at 0.0005 s in computational porous structures with varying pore diameters. As pore size decreases, particle trajectories become more tortuous, accompanied by a decrease in the number of particles passing through the structure within the time frame. (*F*) Flow diffusivity showing the directionality and magnitude of fluid in computational porous structures with varying pore sphericities (aspect ratios). (*G*) Fluid shear rate in various computational porous structures. Shear rate increases with increasing pore diameter and sphericity. (*H*) Particle residence time in various computational porous structures decreases as both pore diameter and sphericity increase. (*I*) Flow diffusivity, represented as the fraction of flow directions at larger degrees than 15°, decreases as both pore diameter and sphericity increase. (*D–I*) In these theoretical models, all flows were confined within the boundary regions and no fluid leaks were allowed. (*J-i*) MicroCT cross-sectional view of porous chitosan pad samples with varying pore sphericities (aspect ratios). (*J-ii*) Whole blood absorption at 3 s after the blood deposition on the surface of samples. (*J-iii*) Microscopic images of the cross-sectional view of human blood plasma-absorbed samples. The blood plasma includes pre-labeled fibrin (green) and platelets (magenta). (*K*) Absorbed volume of whole blood in samples with varying pore sphericities at 10 to 15 s. n = 7. *(*P* < 0.05), **(*P* < 0.01), ***(*P* < 0.001), ****(*P* < 0.0001).

generated less debris compared with gauze-type hemostats with embedded hemostatic powders (*SI Appendix*, Figs. S2C and S3).

We prepared porous structured hemostats with different pore sphericities to validate our simulation models (Fig. 1*J*). Notably, porous chitosan samples with pore sphericity higher than 0.70 absorbed a significantly larger amount of water and whole blood compared to samples with 0.24 and 0.42 sphericities (Fig. 1*K* and *SI Appendix*, Fig. S4). Although the final blood volume absorbed in pore sphericity 0.70 sample was similar to 0.91 and 1.00 samples, the latter two models absorbed quicker than 0.70 sample as shown in Fig. 1 *J, ii*. To further analyze how porous chitosan structure captures and accumulates blood components, we

visualized the distribution of blood clotting components throughout the interior structure of the hemostatic materials. We placed platelet-rich plasma (PRP) isolated from heparinized human blood on the top surface of each hemostat, which was rapidly absorbed into the porous structure of the hemostat and clotted. The microscopic cross-sectional images and quantified data showed that the deposition areas of fibrin and platelets were maximal in pore sphericity 0.91 and 1.00 samples (Fig. 1 *J, iii* and *SI Appendix,* Fig. S4). Pore sphericity values of 0.70, 0.91, and 1.00 also showed dense accumulation of fibrin microthrombi and platelets, allowing for deeper and more extensive penetration of clotting components compared to other samples.

Concentrated Blood Clotting in the Alveolar Chitosan Structure. We next applied the simulation and ex vivo cross-sectional analysis to characterize fluid dynamics and particle movements within existing hemostatic materials (kaolin gauze, chitosan gauze, small oblate porous chitosan) and compared them with our engineered porous chitosan pad (Fig. 2*A*). We extracted the real cross-sectional structures from cryo-sectioned images of different hemostats and conducted simulations on these structures, studying the movement of platelet-sized particles within the void spaces of each hemostatic material. The simulations revealed that fibrous materials could drive a higher fluid shear rate but with a reduced particle residence time (Fig. 2 *B–D* and *SI Appendix,* Fig. S5).

In the following experiments to visualize blood clotting components within the hemostatic materials, the microscopic cross-sectional images and quantified data showed that fibrin microthrombi and platelets were widespread throughout the entire kaolin gauze at sparse density. In the chitosan gauze, fibrin and platelets were more widely distributed along with the horizontal layers, compared to the vertical direction crossing gauze layers, while they were mostly restricted on the surface of small oblate porous chitosan. In contrast, consistent with the simulations, in the case of the porous chitosan pad, deposition of fibrin and platelets showed a radial pattern without preference for longitudinal/transverse directions in a confined area with a high-density level (Fig. 2*E* and *SI Appendix,* Fig. S6). Similarly, when whole blood was deposited on the surface of these hemostats, fibrin thrombi and blood cells predominantly adhered to the fibers in gauze hemostatic materials at a low density, failing to occupy the void space fully. In contrast, in the porous chitosan pads, fibrin thrombi filled the pores, resulting in a denser and more uniform accumulation of fibrin and blood cells (*SI Appendix,* Fig. S7). Inside the porous chitosan pad, activated platelets accumulated near the inner surfaces of the material, alongside fibrin microthrombi filling the pore structures (Fig. 2*F*).

The potential of the porous chitosan pad to accelerate the activation of clotting factors was further examined by measuring the levels of activated factor Xa (FXa) and thrombin generation in heparinized blood after exposure to various hemostatic materials, as these two factors play central roles in converting soluble fibrinogen into insoluble fibrin. The porous chitosan pad exhibited statistically significantly higher FXa activity than chitosan gauze, and statistically significant thrombin generation compared to other control groups (Fig. 2 *G* and *H*). Subsequently, the effect of the porous chitosan pad on FXa activity was further examined in relation to platelet counts. We employed a direct FXa inhibitor (Apixaban) as a negative control and blood plasma with two different platelet counts including PRP and platelet-poor plasma (PPP). In the PRP condition, the porous chitosan pad significantly increased FXa activity even under the Apixaban treatment compared to the control condition. These results indicate the

hemostatic function of our porous chitosan pad has specificity to platelets while it can be triggered with a minimum number of platelets (Fig. 2*I*).

Platelet Interaction with Charged Chitosan Surface. A hemostatic material with a higher affinity to blood clotting components can rapidly capture more of them on the surface, where activated platelets and fibrin clots can propagate the coagulation cascade. Zeta potential measurement showed that the surfaces of chitosan-based hemostats (pad type: 31.03 mV, gauze type: 36.08 mV) exhibited a higher positive charge than kaolin-based hemostat (19.42 mV), while the two major components of the blood clot, fibrinogen (–9.64 mV) and platelets (–10.72 mV), had negatively charged surfaces (Fig. 3*A*).

To isolate surface charge effects from structural influences, various hemostatic materials were pulverized and incorporated into fibrin hydrogel. This hydrogel served as background material (control group) as it had a negative charge, while the pulverized hemostatic materials provided the sole source of positive charge. We employed surface-modified latex microbeads with a net positive or a net negative charge (*SI Appendix,* Fig. S8*A*) and observed the interactions between these beads and composite fibrin hydrogels that incorporated different pulverized hemostat materials. Beads with opposite charges with the composite tend to accumulate on the material surface due to electrostatic attraction, while those with the same charge experience repulsion and are easily removed during the washing process (*SI Appendix,* Fig. S8*B*). When positive hemostatic material was mixed with fibrin gel, it attracted more negatively charged beads. Among them, porous chitosan pad powder in fibrin gel captured significantly more negative beads than the control (*SI Appendix,* Fig. S8 *C* and *E*). In the case of positively charged beads, a slightly higher number of beads remained on the surface of the negatively charged control fibrin gel group compared with other composite fibrin gel groups (*SI Appendix,* Fig. S8 *D* and *E*). Experiments with platelet suspension showed a similar trend, with more negatively charged platelets being trapped on the surface of composite fibrin hydrogel mixed with positively charged hemostatic materials (Fig. 3 *B* and *C*). Notably, despite similar surface charge levels, porous chitosan pad powders captured more negatively charged beads and platelets than chitosan gauze-derived powders when mixed into fibrin hydrogels. This is attributed to the lower density of the porous chitosan pad compared to chitosan gauze (0.12 vs. 1.20 mg/mm^3, *SI Appendix,* Table S1), resulting in a larger volume of chitosan powder being embedded in the composite fibrin hydrogels when equaled by mass, consequently increasing the surface area occupied by chitosan in the gel.

Platelet Activation by Chitosan. Since similarly structured kaolin and chitosan gauzes induced a comparable FXa activity (Fig. 2*G*), we hypothesized that chitosan might also stimulate physiological coagulation cascade like kaolin in contrast to the accepted dogma (9, 10, 15). Platelets were isolated from heparinized human whole blood, and their expression of CD41 (platelet glycoprotein IIb) and CD61 (platelet glycoproteins IIIa) was confirmed by flow cytometry (*SI Appendix,* Fig. S9). Activated platelets can be identified by CD62p (P-selectin) marker, phosphatidylserine (PtSer) exposed to its outer surface, which acts as a binding site for multiple coagulation factors leading to thrombin generation (26, 27), and/or a conformational change of integrin $\alpha_{IIb}\beta_3$ on its surface into a high-affinity state that leads to platelet aggregation (28). Since all procoagulant platelets expose PtSer in general (29), the magnitude of PtSer exposure in platelet outer membrane leaflet was detected using fluorochrome-conjugated Annexin V, which binds to externalized PtSer (Fig. 4*A*).
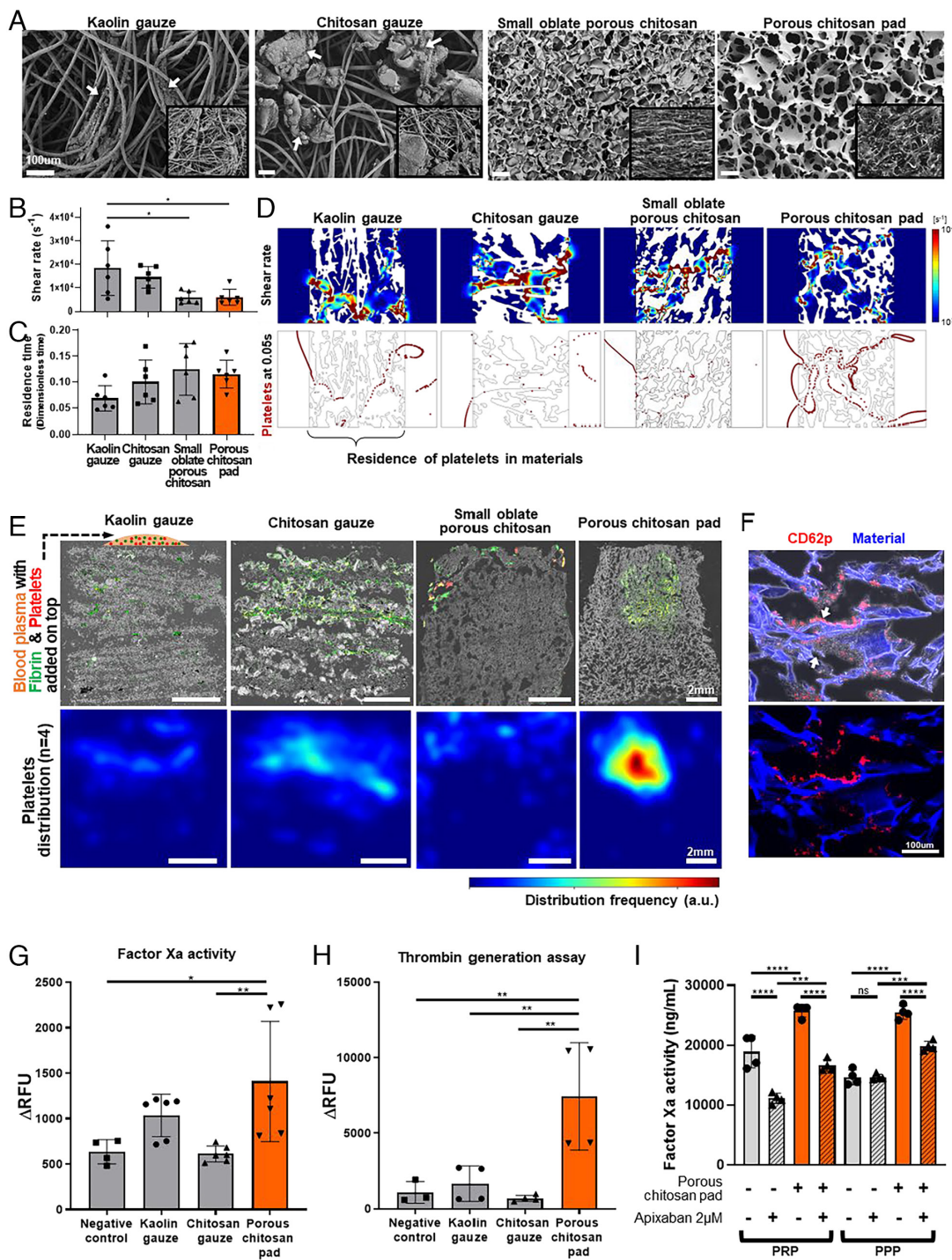
Fig. 2. Porous chitosan pad enables concentrated accumulation of blood clotting components and increases coagulation factors activity. (*A*) FESEM images showing the top-view microstructures of fibrous kaolin gauze, fibrous chitosan gauze, small oblate porous chitosan, and spherical porous chitosan pad. Kaolin or chitosan clumps on the gauze materials were indicated with white arrows. *Inset* images are microCT images of the side-view microstructures of each sample. (*B* and *C*) Simulation results of (*B*) fluid shear rate and (*C*) particle residence time in different hemostatic materials (n = 6). (*D*) Fluid shear rate and platelet distributions within the inner structure of each hemostatic material, simulated by computational fluid dynamic modeling using cross-sectional geometry of hemostatic materials. (*E*) Microscopic cross-sectional images of human blood plasma-absorbed hemostatic materials, with pre-labeled fibrin (green) and platelets (red). Heatmaps show the distribution frequency of platelets in each hemostatic material (n = 4). (*F*) Formation of fibrin microthrombi (arrows) within the pore space of our porous chitosan pad and accumulation of CD62p-labeled activated platelets (red) near the inner surface of the pores. (*G* and *H*) Measurements of FXa activity (*G*) and thrombin generation (*H*) in heparinized blood after exposure to different hemostatic materials (n = 4 to 6). (*I*) Assessment of FXa activity in PRP and PPP following FXa inhibitor (Apixaban) treatment and exposure to a porous chitosan pad (n = 4). (*B* and *C* and *G*–*I*). ns = not significant ($P > 0.05$), *($P < 0.05$), **($P < 0.01$), ***($P < 0.001$), ****($P < 0.0001$).

High-level Annexin V expression of platelets (Annexin V^{Hi}) was increased when they were exposed to chitosan, consistent with activation of platelets (Fig. 4*B*). The significantly increased level of CD62p expression of platelets in the presence of chitosan confirmed the activation of platelets by chitosan (Fig. 4*C*). In addition, the activation of platelet integrin $\alpha_{IIb}\beta_3$ was measured using PAC-1 that binds to the active conformation of the $\alpha_{IIb}\beta_3$ (Fig. 4*D*). Chitosan-exposed platelets showed increased PAC-1 binding in a time-dependent manner, while the control group exhibited negligible binding on its surface.

The cytosolic Ca^{2+} concentration in platelets increases during its activation signaling, which stimulates PtSer-exposing phospholipid scramblase and integrin receptors (29, 30). We visualized this process

using Fluo4 AM reagent, which shows increased fluorescence upon Ca^{2+} binding reactions (Fig. 4*E* and Movies S1 and S2). The fluorescence signal spiked immediately after mixing Fluo4 AM-labeled platelets with chitosan, followed by a decay, probably due to mitochondrial Ca^{2+} uptake (31). In contrast, the control group showed a monotonic fluorescence level throughout the observation. These results indicate chitosan-stimulated CD62p-expressing platelets can exhibit both externalized PtSer and activated integrin $\alpha_{IIb}\beta_3$ via increased intracellular Ca^{2+} concentration.

Chitosan Activates Platelets via TLR2. To understand the underlying interaction mechanism between chitosan and platelets at a molecular level, we validated whether chitosan can directly activate platelets
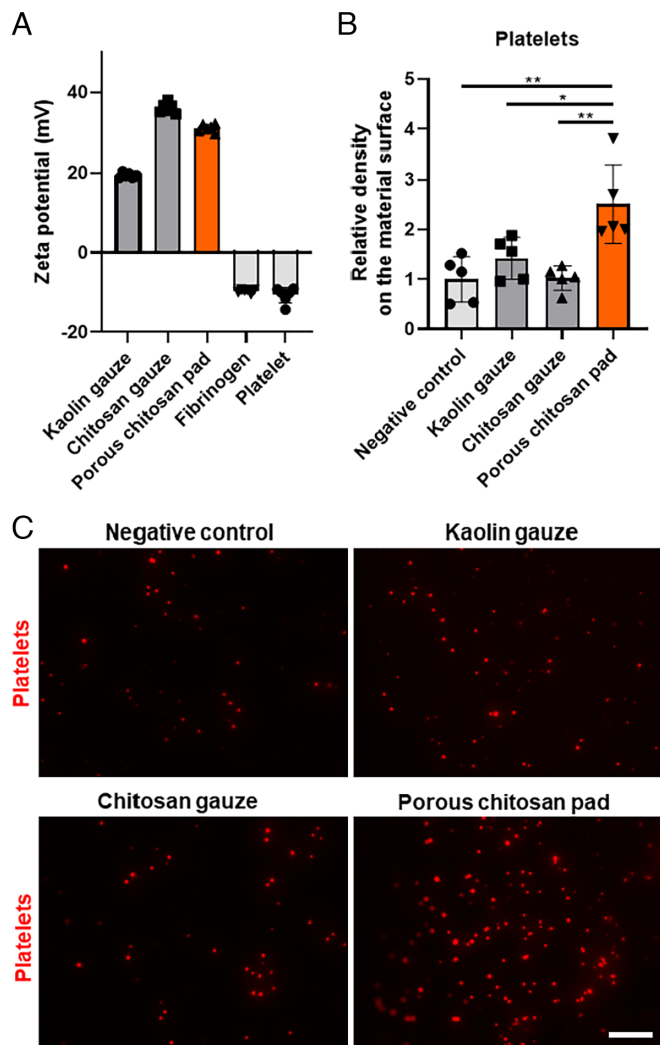
Fig. 3. A positively charged surface of the hemostatic material captures negatively charged platelets. (*A*) Zeta potential values of kaolin- and chitosan-based hemostatic materials, fibrinogen, and platelets (n = 6). (*B*) Relative platelet density (platelet counts per area) on the surface of fibrin gel mixed with pulverized hemostatic materials compared to the control group (n = 5). *($P < 0.05$), **($P < 0.01$). (*C*) Fluorescence microscope images of platelets (red) captured on the surface of fibrin gel mixed with pulverized hemostatic materials.

through receptor binding. We used different pharmacological inhibitors to block representative receptors of platelets involved in major signaling events during platelet activation. Then, we measured the degree of platelet PtSer externalization, which is indicated by Annexin V binding, after exposure to chitosan solution. Specifically, we inhibited integrin $\alpha_{IIb}\beta_3$ receptor (inhibitors: eptifibatide, GR-144053), $P2Y_{12}$ (inhibitors: clopidogrel, cangrelor), PAR (inhibitor for PAR-1: vorapaxar, inhibitor for PAR-4: ML-354), CLEC2 (antibody blocking), and TLR (inhibitor for TLR1/2: CU-CPT22, inhibitor for TLR2: MMG11). As shown in *SI Appendix,* Figs. S10–S12, chitosan activated platelets that were pre-treated to inhibit the function of integrin $\alpha_{IIb}\beta_3$ receptor, $P2Y_{12}$, PARs, and CLEC2, suggesting that a distinct receptor mediated the effects of chitosan. The cyclooxygenase (COX) pathway is another major mechanism involved in platelet activation (32), in addition to the Ca^{2+} signaling cascade. Chitosan-mediated platelet PtSer exposure was not prevented when we applied aspirin, a COX1 inhibitor (*SI Appendix,* Fig. S10G), indicating that chitosan-induced platelet PtSer externalization occurred independently from the COX pathway that involves thromboxane (TxA_2) and TP receptor.

Strikingly, blocking TLR1/2 of platelets with different pharmacological inhibitors, CU-CPT22 and MMG11, abrogated chitosan-mediated PtSer exposure in a dose-dependent manner (Fig. 4 *F* and *G* and *SI Appendix,* Fig. S13), indicating that chitosan stimulates platelets via TLR. Indeed, stimulation of TLR can lead to rapid activation of platelets through increased intracellular Ca^{2+} levels, promoting Ca^{2+}-related downstream signaling (33), consistent with the increased Ca^{2+} signaling seen earlier. We further analyzed whether blocking downstream mechanisms of Ca^{2+} influx could prevent TLR-mediated activation of platelets. We suppressed the increase of intracellular Ca^{2+} concentration of platelets by using a cell-permeable Ca^{2+} chelator (BAPTA) before exposing them to chitosan solution. BAPTA-pretreated platelets showed a significantly reduced Annexin V expression level (Fig. 4*H*). In addition, we confirmed that TLR blocked platelets by CU-CPT22 pretreatment exhibit reduced externalization of integrin $\alpha_{IIb}\beta_3$ based on PAC-1 binding level (*SI Appendix,* Fig. S13C).

To further refine the specificity of chitosan for activating TLR, we employed neutralizing antibodies specific to TLR1 and TLR2. Our results demonstrated a predominant decrease in chitosan-induced platelet activation with TLR2 neutralizing antibody treatment, as shown in the Annexin V assay (Fig. 4*I*), while both types of antibodies effectively inhibited platelet activation in the CD62p assay (Fig. 4*J*). Fig. 4*K* summarizes how chitosan affects platelet activation under the presence of various anticoagulants and anti-platelet agents that do not interact with TLR1/2.

Effective Hemostasis by Porous Chitosan Pad in Various Ex Vivo Bleeding Conditions. A hemostatic material that rapidly absorbs wound exudate and creates a plug by accumulating blood clotting components at the localized area can effectively seal the bleeding site (34). The porous "alveolar" chitosan pad absorbed significantly larger amounts of water and human whole blood faster than kaolin gauze, chitosan gauze, or small oblate porous chitosan (Fig. 5 *A–C*). To assess the clotting capacity of each sample, we measured their blood clotting index (BCI) values, which inversely correlate with the degree of blood coagulation (35–37). Briefly, hemostat samples absorbed blood for 5 min, then were placed in water for another 5 min. Hemoglobin released from ruptured red blood cells, not trapped in clots, was quantified by measuring its light absorbance. The porous chitosan pad released a significantly lower amount of lysed blood (lower BCI) than the other hemostats (Fig. 5 *D* and *E*), indicating that blood clot became a more matured insoluble form in the porous chitosan structure than in other hemostatic materials.

To simulate if our porous chitosan pad could effectively seal the bleeding site and restore the blood flow, we designed a syringe-pump-based fluidic setup where blood flow through the polymeric tubing was disturbed by a hole created on the tube surface, mimicking puncture wound bleeding (Fig. 5*F*). The bleeding rate of this model (2.5 mL/min) corresponds to Grade 1: mild bleeding of the Validated Intraoperative Bleeding Scale (VIBe SCALE) (38). Notably, chitosan-based hemostats required only half of the time to resume the blood flow through tubing compared to the kaolin gauze (Fig. 5*G* and Movies S3–S5). In kaolin gauze, the flow was resumed after complete blood absorption through all layers of material. While both chitosan gauze and the pad showed an equivalent time to resume blood flow, chitosan gauze displayed a wider blood smear pattern than the pad (Fig. 5*H*). The porous chitosan pad exhibited a much more confined smear pattern near the bleeding site (Fig. 5*H*), consistent with our previous results on fibrin and platelet distribution patterns (Fig. 2*E* and *SI Appendix,* Fig. S6). After this ex vivo blood flow experiment, kaolin gauze exhibited the highest hemolysis, followed by chitosan gauze with a significant level of hemolysis.
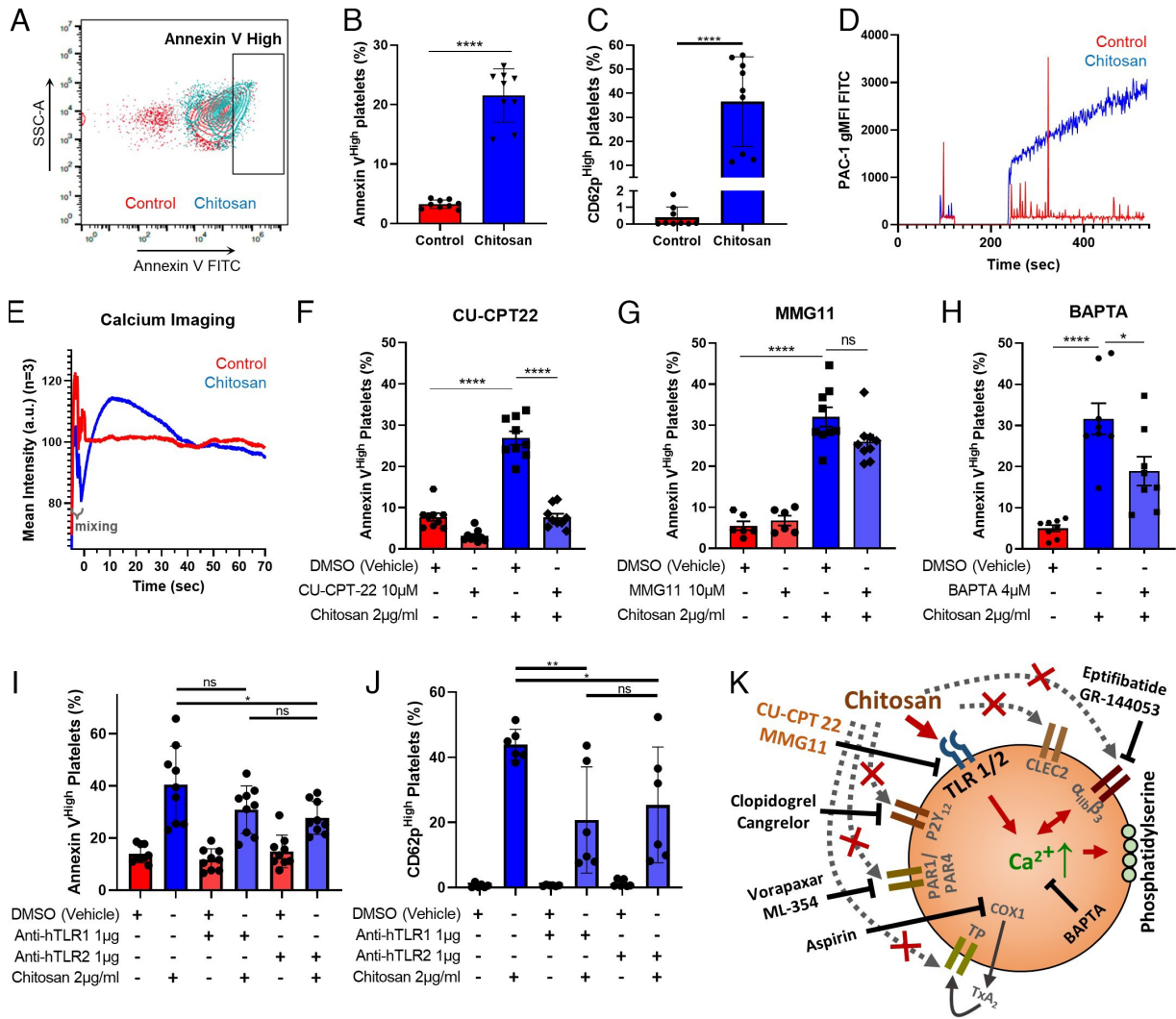
Fig. 4. Chitosan activates platelets via TLR2. (*A*) Representative FACS plot showing chitosan mediated PtSer exposure on platelets, quantified by the Annexin V binding level. Overlaid images show Annexin V High population of platelets in response to the vehicle (1% acetic acid, red) and chitosan solution (2 µg/mL, blue). (*B* and *C*) Quantification of Annexin V (*B*) and CD62p (P-selectin) (*C*) expressions of platelets after exposure to chitosan solution. n = 3 with three replicates per each sample. Unpaired one-tailed *t* test performed (****$P < 0.0001$). (*D*) Quantification of activated integrin αIIbβ3 receptor on platelets based on their binding level to PAC-1, after exposure to chitosan solution. (*E*) A quantified graph (n = 3) showing increased intracellular Ca^{2+} concentration in platelets after exposure to chitosan. Platelets were prelabeled with Ca^{2+} binding fluorescence indicator, Fluo4 AM. (*F–H*) PtSer externalization of chitosan-exposed platelets after pretreatment with various antiplatelet reagents that inhibit different receptors. The degree of platelets with externalized PtSer is presented by the relative percentage of Annexin V High population among total platelets. Platelets were pretreated with (*F*) CU-CPT22, (*G*) MMG11, or vehicles. (*H*) Percentage of Annexin V High cells among total chitosan-exposed platelets after pretreatment with intracellular Ca^{2+} chelator BAPTA. (*I* and *J*) Percentage of Annexin V High (*I*) and CD62p High (*J*) population among total platelets after pretreatment with Anti-hTLR1 or Anti-hTLR2 neutralizing antibodies and treating with/without chitosan. (*F–J*) n = 3 with three replicates per sample. ns = not significant ($P > 0.05$), *($P < 0.05$), **($P < 0.01$), ***($P < 0.001$), ****($P < 0.0001$). (*K*) Schematic representation of chitosan mediated activation of platelets through TLR1/2 and resultant PtSer exposure and integrin αIIbβ3 activation.

In contrast, the porous chitosan pad displayed remarkably low hemolysis (Fig. 5*I*). This result indicates that the porous chitosan pad achieved a superior coagulation level compared to chitosan gauze, despite their comparable hemostasis times.

To assess the efficacy of hemostatic materials under a variety of bleeding conditions, we designed another ex vivo model with a large incision (~5 cm) and higher bleeding rates (35 to 50 mL/min) (Fig. 5*J* and *SI Appendix*, Fig. S14). The bleeding rate of this model can be classified as Grade 3: severe bleeding (>10.0 to 50.0 mL/min) according to the VIBe SCALE (38). When active bleeding began at the incision wound site, a significant pool of blood formed, accompanied by flowing blood streams. Hemostasis was achieved by directly applying both the porous chitosan pad and kaolin gauze to the bleeding site, followed by 1 min of hand compression (Movies S6 and S7). After hemostasis was achieved, observations were made to evaluate for blood leakage under the continuing blood flow at the same rate. Two hemostats, porous chitosan pads and kaolin gauze, maintained

vascular blood flow. However, while porous chitosan pads did not exhibit any blood leakage, repeated blood oozing was observed with kaolin gauze over time (Fig. 5 *J* and *K* and Movies S6 and S7).

Effective Hemostasis in Mouse Liver, and Swine Liver and Carotid Artery Injuries. We next performed in vivo studies on mice treated with anticoagulant heparin and antiplatelet agent clopidogrel to assess the hemostatic efficacy of chitosan-based materials with varying porous structures (Fig. 6*A*). Liver injury models are frequently used in hemostatic research as the liver is a major organ with extensive vascularization, and liver bleeding models can be prepared in a relatively simple and consistent manner compared to other organs to evaluate hemostatic agents in a reproducible manner (39–41). Chitosan-based hemostats prepared in a similar size and shape (*SI Appendix*, Fig. S15A) were gently applied on the bleeding site of mouse liver resection (Fig. 6*B* and *SI Appendix*, Fig. S15 *B–D*). Our porous chitosan pad notably outperformed
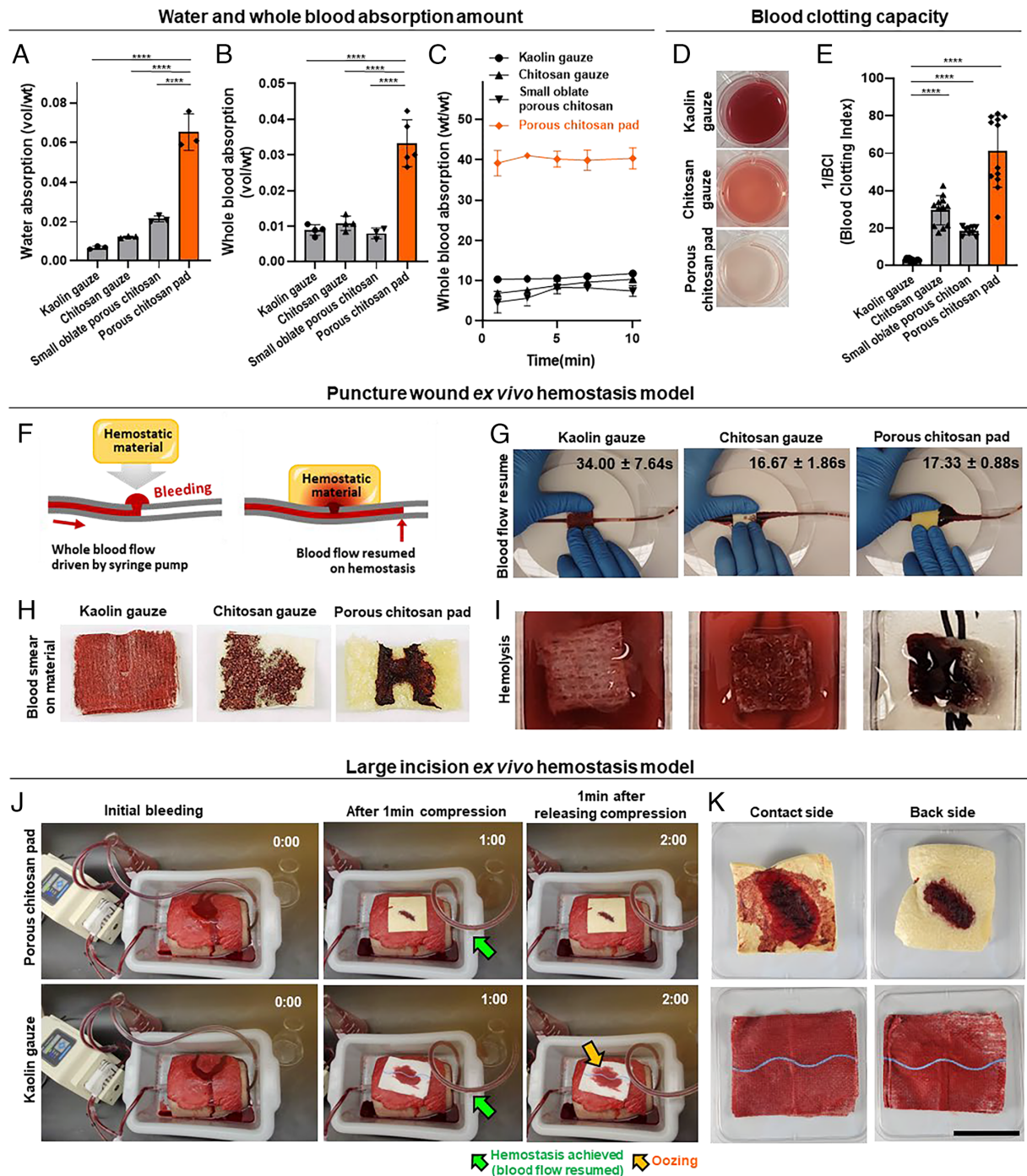
Fig. 5. Blood absorption and ex vivo coagulation capacity of hemostatic materials. (*A* and *B*) The superior capacity of the porous chitosan pad in absorbing water and whole blood compared with kaolin gauze, chitosan gauzes, and small oblate porous chitosan pad (n = 3 to 5). (*C*) The blood absorption of the hemostatic materials over time. (*D* and *E*) Coagulation degree of blood within the hemostatic material, assessed by measuring non-coagulated blood remaining in the material. (*D*) Photo images show non-clotted blood released from hemostatic materials into water after 5 min of clotting. (*E*) BCI represents hemolysis of red blood cells not trapped in the clot. BCI and coagulation level are inversely related. n = 3 to 4 with three replicates per each sample. (*A, B,* and *E*) ****(*P* < 0.0001). (*F*) Schematics of ex vivo puncture wound hemostasis model: Heparinized human whole blood flowed continuously through the tubing, and a hole was created on the surface of the tubing to simulate the bleeding site. Blood flow resumed once a blood plug formed and sealed the hole. (*G*) Ex vivo hemostasis experiment in action. The time shown in each photo indicates the average time ± SD (n = 3) to seal the bleeding hole and resume blood flow in the tubing after applying the hemostatic material. (*H*) Blood smear patterns on the materials after achieving hemostasis. (*I*) Hemolysis evaluation after achieving hemostasis. Black lines indicate the tubing position beneath the hemostats. (*J*) Porous chitosan pad and kaolin gauze were tested on ex vivo hemostasis models with large incisions (~5 cm). Both achieved hemostasis after 1-min hand compression (green arrows), but blood oozing occurred on kaolin gauze during post-hemostasis blood circulation (yellow arrow). (*K*) Blood smear patterns on the materials after achieving hemostasis. (Scale bar, 5 cm.)

negative control (no treatment) and small oblate porous chitosan in achieving faster initial hemostasis (Fig. 6*C*) and reducing post-treatment blood loss (Fig. 6*D*), showing its effective hemostatic capacity under anticoagulant and antiplatelet influence. In this low-scale bleeding setting, the fibrous chitosan hemostatic samples

demonstrated comparable hemostatic efficacy to porous chitosan pad samples as the blood flow lacked sufficient driving force for extensive penetration into the voluminous cavities with the fibrous structure.

Two swine injury models with massive bleeding patterns were also introduced to confirm the in vivo hemostatic effect of the
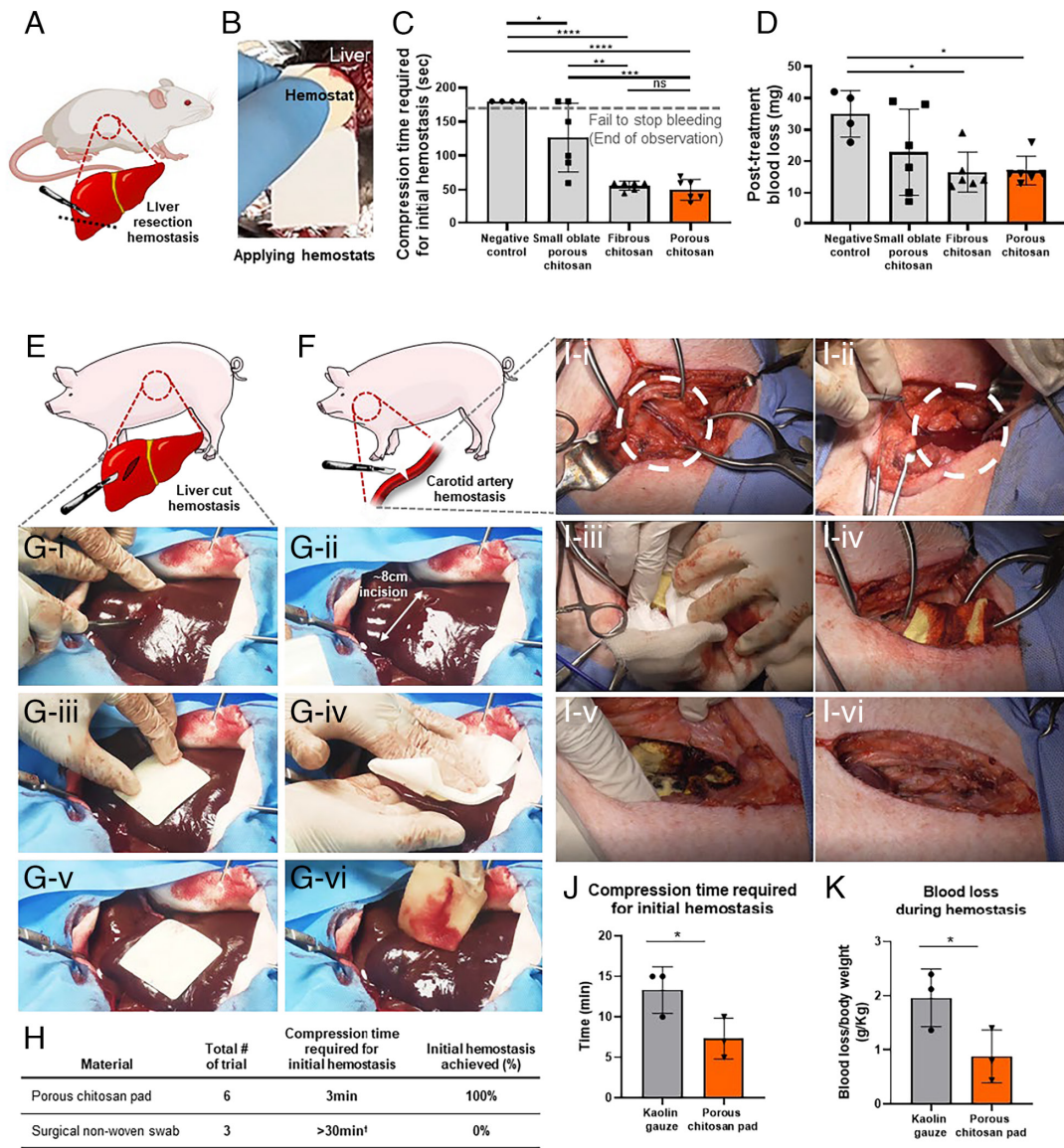
Fig. 6. Hemostatic performance of the porous chitosan pad in animal models. (*A*) Schematics of mouse liver bleeding model. (*B*) A photo image showing the application of a hemostat on the bleeding liver wound site, where the filter paper was placed under the liver to measure the amount of blood loss. (*C*) Compression time required for initial hemostasis using the chitosan-based hemostats. (*D*) Measurements of blood loss following initial hemostasis over a 1-min period. n = 4 for the negative control; n = 6 for each experimental group. (*E* and *F*) Schematics of swine liver and carotid artery injury models. (*G*) Representative photo images of the surgical process for liver cut injury and application of porous chitosan pad: (*G-i* and *G-ii*) ~8 cm liver incision and free bleeding for 30 s; (*G-iii*) Porous chitosan pad applied; (*G-iv*) Hand compression applied for 3 min; (*G-v*) Bleeding stopped and hemostasis maintained; (*G-vi*) Clean wound site after removing the dressing. (*H*) Hemostasis efficacy comparison between porous chitosan pad and surgical non-woven swab gauze on a swine liver injury model. †Bleeding was controlled by electrocautery after 30 min. (*I*) Representative photo images of the surgical process for developing carotid artery injury model in swine and application of porous chitosan pad for hemostasis: (*I-i*) Exposed carotid artery; (*I-ii*) Free bleeding for 30 s; (*I-iii*) Application of porous chitosan pad on the bleeding site and wound packing with a laparotomy sponge; (*I-iv*) Successful hemostasis at 5 to 10 min. There was no blood oozing from the periphery of the dressing; (*I-v*) No bleeding after stopping applying pressure at 120 min. The dressing remained dry, indicating no re-bleeding; (*I-vi*) Clean wound site after removing porous chitosan pad. No residue of hemostatic material was observed. (*J*) Compression time required for initial hemostasis using fibrous kaolin gauze and porous chitosan pad. n = 3 with three replicates per each sample. (*K*) Blood loss during hemostasis using fibrous kaolin gauze and porous chitosan pad. n = 3 with three replicates per each sample. (*C*, *D*, *J*, and *K*) ns = not significant ($P > 0.05$), *($P < 0.05$), **($P < 0.01$), ***($P < 0.001$), ****($P < 0.0001$).

porous chitosan pad (Fig. 6 *E* and *F*). In the swine liver cut model, bleeding occurred at 80 to 120 mL/min rate through a ~8-cm incision. In the carotid hemorrhage model, the initial bleeding rate through the transected carotid artery was >500 mL/min. Both models represented VIBe SCALE Grade 4: life-threatening bleeding (>50 mL/min) (38). The liver cut bleeding model was established by resecting a ~8 cm long incision on the left medial liver lobe. Followed by approximately 60 s of free bleeding, a porous chitosan pad was applied with manual compression and compared with a surgical non-woven swab that is commonly used in the clinic (Fig. 6*G* and Movie S8). The initial bleeding rates recorded within the 60 s of free bleeding were 100.3 ± 14.8 mL/min for

the porous chitosan pad-treated group and 104.6 ± 8.6 mL/min for the surgical swab-treated group. The porous chitosan pad achieved initial hemostasis within 3 min, while all swab gauze trials failed to control the bleeding after 30 min of hand compression (Fig. 6*H*).

A severe carotid artery bleeding model was established under heparin administration by transecting approximately 50% of the circumference of the artery around the neck. After 30 s of continuous bleeding, a porous chitosan pad was applied to the bleeding site and compared with a kaolin gauze that is commonly used in military settings (Fig. 6*I*). While both porous chitosan pad and kaolin gauze successfully stopped the bleeding, the total compression

time to achieve initial hemostasis was significantly lower in the porous chitosan pad group (7.33 ± 1.45 min) than the fibrous kaolin gauze group (13.33 ± 1.67 min) (Fig. 6*J* and Movie S9). In addition, the post-treatment blood loss was significantly reduced in the case of the porous chitosan pad group (0.88 ± 0.28 g/kg) than the fibrous kaolin gauze group (1.96 ± 0.31 g/kg) (Fig. 6*K*). For all groups, there was no bleeding reoccurrence, while all blood vessels treated with hemostatic materials were patent and the physiological and hematological parameters of the pigs were maintained within a normal range (*SI Appendix,* Tables S2–S4).

Hemostasis at the Human Radial Artery Puncture Site. We next evaluated the porous chitosan hemostat in human patients undergoing cardiovascular catheterization procedures. Transradial approach is a widely used technique for coronary angiography and percutaneous coronary intervention procedures (42). As a standard protocol, anticoagulants are administered to patients undergoing diagnostic and therapeutic coronary procedures (43). The use of these anticoagulant agents greatly increases the hemostasis time at the vascular access site after removal of the arterial sheath, and this condition is further exaggerated due to systolic arterial pulsatility (44). Traditional taping and physical compression are effective, but require extensive nursing and patient ambulation time (45). Among various new techniques (46, 47), topical hemostatic dressings with clot-promoting components have shown significant promise, providing efficient control over moderate to severe bleeding (48–50).

In this clinical study, the porous chitosan pad was applied for managing puncture site bleeding at the radial artery after cardiac catheterization (Fig. 7*A*). No device failure was observed in any patient, and successful hemostasis was achieved with the use of a single dressing. The porous chitosan pad consistently achieved hemostasis within an average time frame of 5.56 ± 1.36 min for all patients, demonstrating its effectiveness across diabetic, hypertensive, and fibrinolytic therapy cases (*SI Appendix,* Table S5). Importantly, hemostasis was reliably attained within 9 min for all patients, even in cases with heparin doses as high as 12,500 IU. When categorizing the data by heparin dose, we observed successful hemostasis within mean times of 4.96 ± 1.12 min for low doses and 6.78 ± 0.92 min for high doses (Fig. 7*B*). Furthermore, the pad was easy to apply and remove, receiving high patient comfort scores (Fig. 7 *C* and *D*).

Discussion

The changes in societal dynamics and the evolution in anticoagulants now pose clinical challenges that highlight the limits of hemostats that were developed in the past century. In this study, we address these limits by rationally integrating a systematic understanding of coagulation mechanisms from the macro structural level to the molecular scale (Fig. 8). We demonstrate that an architecturally optimized hemostat that activates a distinct yet undrugged molecular mechanism of coagulation can emerge as an effective hemostat in the setting of massive vascular injuries and on anticoagulant therapies.

Our study highlights the impact of architectural design in developing next-generation hemostats. While several studies have investigated chitosan-based hemostats, the focus was primarily on the intrinsic properties of the chitosan source materials or their chemical modifications (51, 52). Although such chemical alterations often result in changes to pore morphology (53, 54), the influence of these structural transformations has not been sufficiently explored. We found that the shape of pores indeed plays a crucial role in driving blood flow into hemostatic materials and accumulating clotting components within the materials. Additionally, the highly positively charged surface of chitosan effectively captured negatively charged platelets, which can accelerate the subsequent coagulation processes. Taken together, optimized porous structure of the chitosan pad augments the interaction between chitosan and platelets, by achieving a balance between swift fluid absorption, which delivers more platelets, and the creation of tortuous paths within the structure to maximize platelet-material engagement and the formation of highly condensed and matured platelet plugs.

Our study challenges a current dogma that chitosan does not impact the coagulation cascade. We observed that chitosan could specifically activate TLR2 of platelets, which triggered an elevation of Ca^{2+} influx and externalization of PtSer toward the outer membrane, which is known to facilitate binding of clotting factors (55), and makes the platelet surface charge into a more negative state (56). Indeed, our finding of platelet activation by chitosan via TLR2 is consistent with the observations of chitin oligomers directly binding to TLR2 on macrophages and inducing immune activation, where chitin shares the same acetylated monomer unit with chitosan (57). This finding attains significance as TLR2 remains an undrugged target in the coagulation machinery, which means that activating this mechanism of action could lead to hemostasis independent of any of the current anticoagulant treatments. Indeed, in vivo studies on mice co-administered with heparin and clopidogrel revealed that the porous chitosan pad effectively mitigated bleeding, even under anticoagulant and antiplatelet influence (Fig. 6 *A–D*). Additionally, we observed substantially reduced hemostasis time and blood loss compared to other hemostats in our ex vivo and large animal studies covering a range of bleeding severities (38) and in the presence of heparin, which highlights its potential use in different clinical settings, including surgical and trauma.
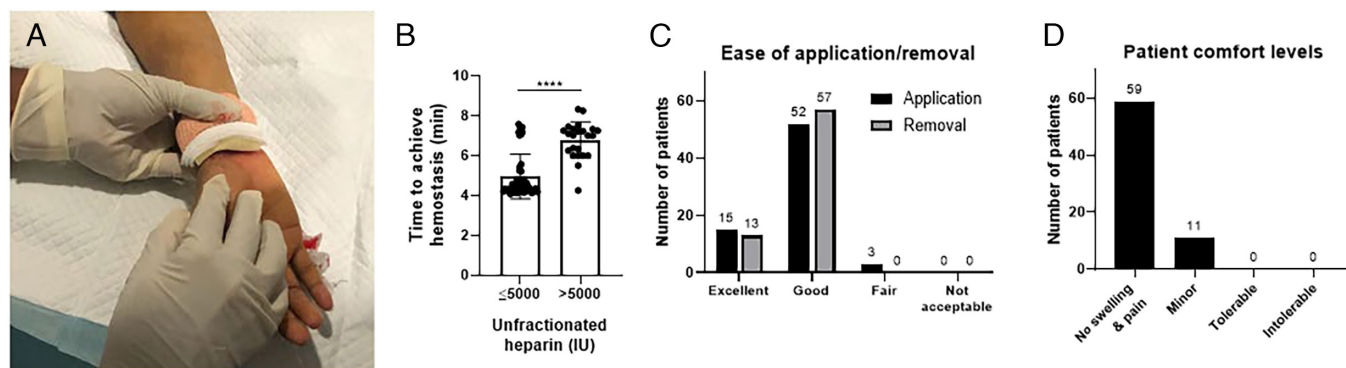

Fig. 7. Hemostatic performance of the porous chitosan pad in a clinical study. (*A*) A photo image showing the application of a porous chitosan pad for radial artery hemostasis after cardiac catheterization. (*B*) Time to achieve hemostasis when porous chitosan pad was applied to the radial artery puncture sites. n = 47 (≤5,000), n = 23 (>5,000). ****(*P* < 0.0001). (*C*) Survey results on the ease of application and removal of porous chitosan pad on the bleeding site of the radial artery. (*D*) Patient comfort level survey results when porous chitosan pad used for radial artery hemostasis.
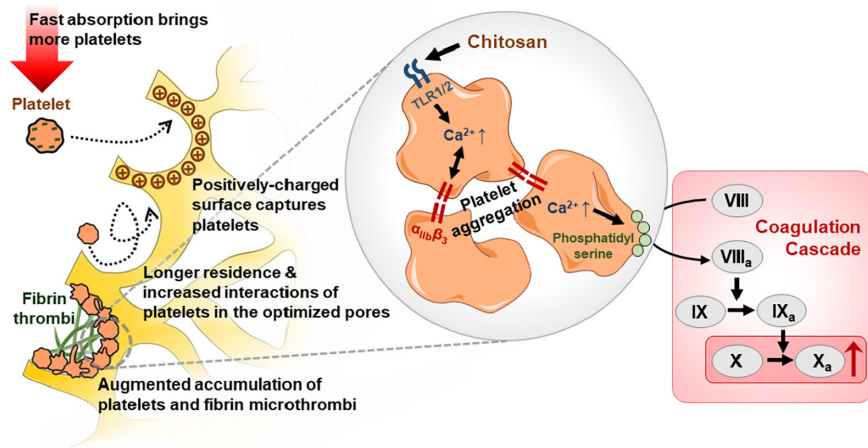
Fig. 8. Schematics illustrating key hemostatic mechanisms of the porous chitosan pad. The tortuous porous microstructure allows for rapid absorption of blood, transporting more platelets into the material. Negatively charged platelets, brought closely to the material surface, are captured and accumulated by the positively charged chitosan surface. In addition, the porous geometry of chitosan material can prolong the platelet residence time within its structure and increase the interaction between platelet and chitosan material, resulting in enhanced accumulation of platelets and fibrin microthrombi. At the molecular scale, chitosan can activate the TLR2 of platelet, which increases calcium influx that leads to PtSer exposure and integrin αIIbβ3 activation, boosting coagulation cascade. All these mechanisms synergistically improve the hemostatic performance of the porous chitosan pad.

Several aspects of the porous hemostat can facilitate its use in humans. First, our clinical study shows that the porous chitosan hemostat achieved hemostasis within 9 min in 100% of patients undergoing radial artery catheterization under high-dosage heparin treatment. This compares favorably to commonly used assisted compression devices, such as the TR band, which necessitate over 2 h of compression for hemostasis, or using other materials like kaolin gauze and alternative chitosan-based pads, which despite reducing compression time, still require over 30 min (48–50). Indeed, at heparin doses of 5,000 to 12,500 IU, the porous chitosan pad achieved a hemostasis time of 5.4 ± 1.4 min, similar to that previously reported by Arbel et al. with the HemCon® chitosan-based hemostat pad (58) using 2,500 IU of heparin. Second, with an increasing population being put on maintenance anticoagulant therapies, there is an emerging segment of patients who will need a hemostat that activates coagulation via a new mechanism. However, we should also highlight that with TLR inhibitors in the pipeline for treating immunological conditions (59), there is an ongoing necessity to evolve next-generation materials capable of activating distinct coagulation mechanisms for effective hemostasis. Similarly, the role of TLR2 polymorphism in platelet activation needs further studies, as it may also have an impact on the overall outcome. Finally, we engineered the chitosan hemostatic pad with optimized porous structures using a slow-freezing technique. Interestingly, this single-phase engineering design overcame the limitation of debris and dislodgement of powder from classical hemostat. Further fine-tuning of the microstructures can be accomplished using other advanced techniques, such as directional freezing (60), or by introducing composites with other materials (61). Exploring hierarchical porous structures (62, 63) or hybrid structures (64), which incorporate a strategic mix of high absorption-low accumulation structures alongside low absorption-high accumulation ones, can also offer further opportunities to enhance hemostatic efficacy. Indeed, the integration of architecture, engineering, and the molecular understanding of materials-biology interactions is critical to the continual development of next-generation hemostats.

Materials and Methods

The materials and detailed procedures of fabrication of porous chitosan pad, FESEM, microCT, finite element model simulation, zeta potential measurements, assessment of electrostatic charge effect using microbead and platelet collection platform, thrombin and FXa assays, calcium imaging, water/blood absorption and BCI measurements, cryosectioning and quantification of sectioned samples, platelet flow cytometry, puncture wound ex vivo hemostasis, large incision ex vivo hemostasis, mouse liver bleeding model, swine liver injury model, swine carotid artery injury model, radial artery hemostasis after cardiac catheterization, and statistical analysis are provided in *SI Appendix, Materials and Methods* section.

Data, Materials, and Software Availability. All analysis codes are available at: https://doi.org/10.7910/DVN/ZWKPEB (65). All other data are included in the article and/or supporting information.

Author affiliations: ᵃCenter for Engineered Therapeutics, Brigham and Women's Hospital, Harvard Medical School, Boston, MA 02115; ᵇDivision of Rheumatology, Inflammation and Immunity, Department of Medicine, Brigham and Women's Hospital, Harvard Medical School, Boston, MA 02115; ᶜDepartment of Orthopaedic Surgery, Brigham and Women's Hospital, Harvard Medical School, Boston, MA 02115; ᵈDivision of Health Sciences and Technology, Harvard–Massachusetts Institute of Technology, Massachusetts Institute of Technology, Cambridge, MA 02139; ᵉDepartment of Translational Dental Medicine, Boston University Henry M. Goldman School of Dental Medicine, Boston, MA 02118; ᶠDepartment of Veterinary Pharmacology and Toxicology, College of Veterinary Science, P. V. Narasimha Rao Telangana Veterinary University, Hyderabad 500030, India; ᵍCare Institute of Medical Sciences, Ahmedabad 380060, India; ʰAxio Biosolutions Private Limited, Ahmedabad 382220, India; ⁱAdvamedica Inc., Boston, MA 02138; and ʲNational Chemical Laboratories, Pune 411021, India

Author contributions: V.K.L., T.L., A.G., T.S., M.V.B., K.K.B., M.C., K.P., P.B., B.N., G.V., A.A., K.S., L.M., S.S., R.A.M., and H.L.J. designed research; V.K.L., T.L., A.G., T.S., M.V.B., K.K.B., M.C., K.P., P.B., B.N., G.V., A.A., K.S., and L.M. performed research; L.M. contributed new reagents/analytic tools; V.K.L., T.L., A.G., T.S., M.B., M.C., K.P., P.B., B.N., A.A., K.S., L.M., S.S., R.A.M., and H.L.J. analyzed data; and V.K.L., T.L., A.G., A.A., K.S., L.M., S.S., R.A.M., and H.L.J. wrote the paper.

Reviewers: B.B., University of Notre Dame; and K.M., Wayne State University.

1. K. Brohi, R. L. Gruen, J. B. Holcomb, Why are bleeding trauma patients still dying? *Intensive Care Med.* **45**, 709–711 (2019).
2. E. R. Donley, J. W. Loyd, *Hemorrhage Control* (StatPearls Publishing, 2018).
3. M. Melkonian *et al.*, Bleeding risk of antiplatelet drugs compared with oral anticoagulants in older patients with atrial fibrillation: A systematic review and meta-analysis. *J. Thromb. Haemost.* **15**, 1500–1510 (2017).
4. M. A. Crowther, T. E. Warkentin, Bleeding risk and the management of bleeding complications in patients undergoing anticoagulant therapy: Focus on new anticoagulant agents. *Blood* **111**, 4871–4879 (2008).
5. J. McManus, T. Hurtado, A. Pusateri, K. J. Knoop, A case series describing thermal injury resulting from zeolite use for hemorrhage control in combat operations. *Prehosp. Emerg. Care* **11**, 67–71 (2007).

6. A. I. Geller, N. Shehab, M. C. Lovegrove, N. J. Weidle, D. S. Budnitz, Bleeding related to oral anticoagulants: Trends in US emergency department visits, 2016–2020. *Thromb. Res.* **225**, 110–115 (2023).

7. H. T. Peng, Hemostatic agents for prehospital hemorrhage control: A narrative review. *Mil. Med. Res.* **7**, 1–18 (2020).

8. M. C. Neuffer *et al.*, Hemostatic dressings for the first responder: A review. *Mil. Med.* **169**, 716–720 (2004).

9. B. L. Bennett, L. Littlejohn, Review of new topical hemostatic dressings for combat casualty care. *Mil. Med.* **179**, 497–514 (2014).

10. A. H. Smith, C. Laird, K. Porter, M. Bloch, Haemostatic dressings in prehospital care. *Emerg. Med. J.* **30**, 784–789 (2013).

11. J. H. Griffin, C. G. Cochrane, Mechanisms for the involvement of high molecular weight kininogen in surface-dependent reactions of Hageman factor. *Proc. Natl. Acad. Sci. U.S.A.* **73**, 2554–2558 (1976).

12. Q. Z. Wang *et al.*, Preparation and blood coagulation evaluation of chitosan microspheres. *J. Mater. Sci. Mater. Med.* **19**, 1371–1377 (2008).

13. S. B. Rao, C. P. Sharma, Use of chitosan as a biomaterial: Studies on its safety and hemostatic potential. *J. Biomed. Mater. Res.* **34**, 21–28 (1997).

14. B. S. Kheirabadi *et al.*, Safety evaluation of new hemostatic agents, smectite granules, and kaolin-coated gauze in a vascular injury wound model in swine. *J. Trauma Acute Care Surg.* **68**, 269–278 (2010).

15. H. Hattori, M. Ishihara, Changes in blood aggregation with differences in molecular weight and degree of deacetylation of chitosan. *Biomed. Mater.* **10**, 015014 (2015).

16. Y. Zhong *et al.*, Application and outlook of topical hemostatic materials: A narrative review. *Ann. Transl. Med.* **9**, 577 (2021).

17. W. S. Nesbitt *et al.*, A shear gradient–Dependent platelet aggregation mechanism drives thrombus formation. *Nat. Med.* **15**, 665–673 (2009).

18. Z. M. Ruggeri, J. N. Orje, R. Habermann, A. B. Federici, A. J. Reininger, Activation-independent platelet adhesion and aggregation under elevated shear stress. *Blood* **108**, 1903–1910 (2006).

19. Y. Cui *et al.*, Smart sponge for fast liquid absorption and thermal responsive self-squeezing. *Adv. Mater.* **32**, 1908249 (2020).

20. L. Wang *et al.*, A natural polymer-based porous sponge with capillary-mimicking microchannels for rapid hemostasis. *Acta Biomat.* **114**, 193–205 (2020).

21. X. Du *et al.*, Microchannelled alkylated chitosan sponge to treat noncompressible hemorrhages and facilitate wound healing. *Nat. Commun.* **12**, 1–16 (2021).

22. N. Nejatishahidein, A. L. Zydney, Depth filtration in bioprocessing–New opportunities for an old technology. *Curr. Opin. Chem. Eng.* **34**, 100746 (2021).

23. M. Y. Kim, J. Lee, Chitosan fibrous 3D networks prepared by freeze drying. *Carbohydr. Polym.* **84**, 1329–1336 (2011).

24. K. Yin, P. Divakar, U. G. K. Wegst, Freeze-casting porous chitosan ureteral stents for improved drainage. *Acta Biomater.* **84**, 231–241 (2019).

25. B. Simpson, N. Gagne, M. Simpson, "Bioprocessing of chitin and chitosan" in *Fisheries Processing*, A. M. Martin, Ed. (Springer, 1994), pp. 155–173.

26. G. E. Gilbert, D. Drinkwater, S. Barter, S. Clouse, Specificity of phosphatidylserine-containing membrane binding sites for factor VIII. Studies with model membranes supported by glass microspheres (lipospheres). *J. Biol. Chem.* **267**, 15861–15868 (1992).

27. E. M. Bevers, P. L. Williamson, Getting to the outer leaflet: Physiology of phosphatidylserine exposure at the plasma membrane. *Physiol. Rev.* **96**, 605–645 (2016).

28. N. Rukoyatkina *et al.*, Phosphatidylserine surface expression and integrin αIIbβ3 activity on thrombin/convulxin stimulated platelets/particles of different sizes. *Br. J. Haematol.* **144**, 591–602 (2009).

29. N. Abbasian, S. L. Millington-Burgess, S. Chabra, J.-D. Malcor, M. T. Harper, Supramaximal calcium signaling triggers procoagulant platelet formation. *Blood Adv.* **4**, 154–164 (2020).

30. S.-J. Joo, Mechanisms of platelet activation and integrin αIIbβ3. *Korean Circ. J.* **42**, 295–301 (2012).

31. S. I. Obydennyy, A. N. Sveshnikova, F. I. Ataullakhanov, M. A. Panteleev, Dynamics of calcium spiking, mitochondrial collapse and phosphatidylserine exposure in platelet subpopulations during activation. *J. Thromb. Haemost.* **14**, 1867–1881 (2016).

32. N. Khan, A. D. Farooq, B. Sadek, Investigation of cyclooxygenase and signaling pathways involved in human platelet aggregation mediated by synergistic interaction of various agonists. *Drug Des. Devel. Ther.* **9**, 3497 (2015).

33. K. Fälker, K. Klarström-Engström, T. Bengtsson, T. L. Lindahl, M. Grenegård, The toll-like receptor 2/1 (TLR2/1) complex initiates human platelet activation via the src/Syk/LAT/PLCγ2 signalling cascade. *Cell. Signal.* **26**, 279–286 (2014).

34. H. Khoshmohabat, S. Paydar, H. M. Kazemi, B. Dalfardi, Overview of agents used for emergency hemostasis. *Trauma Mon.* **21**, e26023 (2016).

35. X. Cheng *et al.*, Isolation, characterization and evaluation of collagen from jellyfish Rhopilema esculentum Kishinouye for use in hemostatic applications. *PLoS One* **12**, e0169731 (2017).

36. Y.-W. Wang *et al.*, Biological effects of chitosan-based dressing on hemostasis mechanism. *Polymers* **11**, 1906 (2019).

37. W. Chen *et al.*, A composite hydrogel based on pectin/cellulose via chemical cross-linking for hemorrhage. *Front. Bioeng. Biotechnol.* **8**, 627351 (2021).

38. K. M. Lewis *et al.*, Development and validation of an intraoperative bleeding severity scale for use in clinical studies of hemostatic agents. *Surgery* **161**, 771–781 (2017).

39. B. M. Mohammed, D. M. Monroe, D. Gailani, Mouse models of hemostasis. *Platelets* **31**, 417–422 (2020).

40. A. E. Pusateri *et al.*, Advanced hemostatic dressing development program: Animal model selection criteria and results of a study of nine hemostatic dressings in a model of severe large venous hemorrhage and hepatic injury in Swine. *J. Trauma* **55**, 518–526 (2003).

41. V. A. Paternò, A. Bisin, A. Addis, Comparison of the efficacy of five standard topical hemostats: A study in porcine liver and spleen models of surgical bleeding. *BMC Surg.* **20**, 1–10 (2020).

42. G. Ando, D. Capodanno, Radial versus femoral access in invasively managed patients with acute coronary syndrome: A systematic review and meta-analysis. *Ann. Intern. Med.* **163**, 932–940 (2015).

43. J. M. ten Berg, H. T. Plokker, F. W. Verheugt, Antiplatelet and anticoagulant therapy in elective percutaneous coronary intervention. *Curr. Control Trials Cardiovasc. Med.* **2**, 129–140 (2001).

44. D. Baric, Why pulsatility still matters: A review of current knowledge. *Croat. Med. J.* **55**, 609–620 (2014).

45. K. Yun, W. Jeon, B. Kang, G. Kim, Effectiveness of a compressive device in controlling hemorrhage following radial artery catheterization. *Clin. Exp. Emerg. Med.* **2**, 104–109 (2015).

46. F. Poretti, T. Rosen, B. Körner, D. Vorwerk, Chitosan pads vs. manual compression to control bleeding sites after transbrachial arterial catheterization in a randomized trial. *Rofo* **177**, 1260–1266 (2005).

47. S. Rathore *et al.*, A randomized comparison of TR band and radistop hemostatic compression devices after transradial coronary intervention. *Catheter. Cardiovasc. Interv.* **76**, 660–667 (2010).

48. N. Dai *et al.*, A comparison of 2 devices for radial artery hemostasis after transradial coronary intervention. *J. Cardiovasc. Nurs.* **30**, 192–196 (2015).

49. J. S. Roberts, J. Niu, J. A. Pastor-Cervantes, Comparison of hemostasis times with a chitosan-based hemostatic pad (Clo-SurPlus Radial™) vs mechanical compression (TR band®) following transradial access: A pilot study. *Cardiovasc. Revasc. Med.* **20**, 871–874 (2019).

50. J. S. Roberts, J. Niu, J. A. Pastor-Cervantes, Comparison of hemostasis times with a kaolin-based hemostatic pad (QuikClot radial) vs mechanical compression (TR band) following transradial access: A pilot prospective study. *J. Invasive Cardiol.* **29**, 328–334 (2017).

51. A. E. Pusateri *et al.*, Effect of a chitosan-based hemostatic dressing on blood loss and survival in a model of severe venous hemorrhage and hepatic injury in swine. *J. Trauma Acute Care Surg.* **54**, 177–182 (2003).

52. G. P. De Castro *et al.*, Determination of efficacy of novel modified chitosan sponge dressing in a lethal arterial injury model in swine. *J. Trauma Acute Care Surg.* **72**, 899–907 (2012).

53. D. E. L. Angulo, P. J. do Amaral Sobral, The effect of processing parameters and solid concentration on the microstructure and pore architecture of gelatin-chitosan scaffolds produced by freeze-drying. *Mater. Res.* **19**, 839–845 (2016).

54. F. Saporito *et al.*, Freeze dried chitosan acetate dressings with glycosaminoglycans and traxenamic acid. *Carbohydr. Polym.* **184**, 408–417 (2018).

55. N. N. Topalov *et al.*, Two types of procoagulant platelets are formed upon physiological activation and are controlled by integrin αIIbβ3. *Arterioscler. Thromb. Vasc. Biol.* **32**, 2475–2483 (2012).

56. T. Brzoska, Y. Suzuki, H. Mogami, H. Sano, T. Urano, Binding of thrombin-activated platelets to a fibrin scaffold through αIIbβ3 evokes phosphatidylserine exposure on their cell surface. *PLoS One* **8**, e55466 (2013).

57. K. Fuchs *et al.*, The fungal ligand chitin directly binds TLR 2 and triggers inflammation dependent on oligomer size. *EMBO Rep.* **19**, e46065 (2018).

58. J. Arbel *et al.*, USage of chitosan for Femoral (USF) haemostasis after percutaneous procedures: A comparative open label study. *EuroIntervention* **6**, 1104–1109 (2011).

59. E. J. Hennessy, A. E. Parker, L. A. J. O'Neill, Targeting toll-like receptors: Emerging therapeutics? *Nat. Rev. Drug Discov.* **9**, 293–307 (2010).

60. L. Qian, H. Zhang, Controlled freezing and freeze drying: A versatile route for porous and micro-/nano-structured materials. *J. Chem. Technol. Biotechnol.* **86**, 172–184 (2011).

61. M. A. Khan, M. Mujahid, A review on recent advances in chitosan based composite for hemostatic dressings. *Int. J. Biol. Macromol.* **124**, 138–147 (2019).

62. J. Li *et al.*, Chitosan/diatom-biosilica aerogel with controlled porous structure for rapid hemostasis. *Adv. Healthc. Mater.* **9**, 2000951 (2020).

63. H. L. Jang *et al.*, Biofunctionalized ceramic with self-assembled networks of nanochannels. *ACS Nano* **9**, 4447–4457 (2015).

64. E. Nyberg, A. O'Sullivan, W. Grayson, ScafSlicr: A MATLAB-based slicing algorithm to enable 3D-printing of tissue engineering scaffolds with heterogeneous porous microarchitecture. *PLoS One* **14**, e0225007 (2019).

65. V. Lee *et al.*, Data for "An architecturally rational hemostat for rapid stopping of massive bleeding on anticoagulation therapy". Harvard Dataverse. https://doi.org/10.7910/DVN/ZWKPEB. Deposited 3 January 2024.